

PAPER

Stretchability of PMMA-supported CVD graphene and of its electrical contacts

To cite this article: Hongwoo Jang *et al* 2020 *2D Mater.* **7** 014003

View the [article online](#) for updates and enhancements.



PAPER

Stretchability of PMMA-supported CVD graphene and of its electrical contacts

RECEIVED
2 May 2019REVISED
1 August 2019ACCEPTED FOR PUBLICATION
8 October 2019PUBLISHED
29 October 2019Hongwoo Jang¹, Zhaohe Dai², Kyoung-Ho Ha³, Shideh Kabiri Ameri^{4,5} and Nanshu Lu^{1,2,6,7}¹ Texas Materials Institute, University of Texas at Austin, Austin, TX, United States of America² Department of Aerospace Engineering and Engineering Mechanics, University of Texas at Austin, Austin, TX, United States of America³ Department of Mechanical Engineering, University of Texas at Austin, Austin, TX, United States of America⁴ Department of Electrical and Computer Engineering, University of Texas at Austin, Austin, TX, United States of America⁵ Department of Electrical and Computer Engineering, Queen's University, Kingston, ON, Canada⁶ Department of Biomedical Engineering, University of Texas at Austin, Austin, TX, United States of America⁷ Author to whom any correspondence should be addressed.E-mail: nanshulu@utexas.edu**Keywords:** graphene, PMMA, stretchability, fracture, cyclicSupplementary material for this article is available [online](#)**Abstract**

The remarkable mechanical robustness and excellent electrical/thermal properties make graphene a promising candidate for future flexible, stretchable and bio-integrated electronics. In practice, many soft electronics such as the graphene electronic tattoos (GETs) demand the chemical vapor deposited (CVD) graphene to be supported by a deformable substrate. Moreover, various conductive overlayers need to directly laminate on graphene to make electrical contacts. To investigate the mechanical reliability of CVD graphene in these situations, we fabricated CVD monolayer graphene supported by ultrathin poly(methyl methacrylate) (PMMA) substrate and also placed gold/polyethylene terephthalate (Au/PET) and graphene/PMMA (Gr/PMMA) overlayers on graphene. The stretchability of the Gr/PMMA and the overlayer-Gr/PMMA interface was characterized by electrical resistance change during uniaxial tensile tests. Combined with *in situ* microstructure and Raman investigation, we identified four deformation/fracture stages of Gr/PMMA—pre-cracking elastic deformation, limited micro-cracking in graphene, extensive cracking in graphene, and macro-cracking in PMMA. While micro-cracks emerged in graphene at very small strain (~0.9%), the electrical conductivity of the Gr/PMMA specimen remained up to tensile strains of ~14.5%. In contrast, 100 nm-thick Au film supported by the same PMMA substrate fully ruptured after tensile strains of ~1%. When laminating Au/PET and Gr/PMMA over Gr/PMMA, we found that the Au/PET-Gr/PMMA interface is very vulnerable but the Gr/PMMA-Gr/PMMA interface behaves very similar to intact Gr/PMMA electromechanically. The cyclic behaviour of Gr/PMMA, the effects of PMMA thickness and adhesion are also briefly discussed. The present experimental study provides fundamental insight into the failure of ultrathin polymer-supported graphene and its electrical contacts, which is critical for designing future graphene-based soft electronics.

1. Introduction

Emerging flexible and stretchable electronics technologies are expected to disrupt many conventional devices such as displays [1], robotics [2, 3], wearables [4, 5], implantables [6], energy generators [7], etc attributing to their thinness, softness, ruggedness and lightweight. Particularly important in this field is to develop materials and structures that can maintain electronic functionality under

large, cyclic deformations. Besides structurally designing conventional semiconducting and metallic materials into stretchable shapes [8], intrinsically deformable functional nanomaterials emerge as popular alternatives [6, 9]. Nanomaterials used in soft electronics include carbon nanotubes (CNTs) [10–12], metal nanowires (NWs) [13, 14], two-dimensional (2D) materials [15–17], and many more. Among them, graphene is the thinnest material (0.34 nm) that is also highly conductive both electrically and

thermally, optically transparent, mechanically robust, biocompatible, and potentially low cost [18–21]. As a result, graphene has been widely applied as the electrode material in soft electronics, optics, sensors, and energy devices [22, 23] as well as the thermal dissipator for power devices [24, 25].

While each of these applications exploits a different fundamental property of graphene, they all depend on its mechanical integrity for structural reliability and device performances [26–31]. The mechanical behaviors of suspended graphene have been well studied [18, 32, 33]. Through nanoindentation, the pioneering work by Lee *et al* found the pristine monocrystalline graphene to be the strongest material ever measured [18]. Specifically, the Young's modulus of pristine graphene is found to be ~ 1 TPa, with a strength that can approach 130 GPa, and a surprising fracture strain up to 25% [18]. Defective graphene is more commonly used for electronics since graphene made with scalable fabrication techniques inevitably contain defects such as grain boundary, vacancies, and so on [34]. Interestingly, defects such as vacancies and oxygen-containing groups can even make graphene more damage-tolerant at least in the nanoindentation tests [35, 36].

In practice, graphene is most often supported by a deformable substrate in soft (i.e. flexible and stretchable) electronic devices [23, 37]. Therefore, the stretchability of polymer-supported CVD graphene has also been studied. Table 1 summarizes available results in the literature [38–44]. In this table, we only focus on CVD graphene sheets although there exist other forms of CVD graphene, such as graphene foam [45], graphene nanowalls [46], graphene scrolls [44], and graphene woven fabrics [47], etc. Depending on the type of substrate, the number of graphene layers, the boundary condition, and the criterion to extract stretchability, the reported stretchability of graphene vary significantly, from 2% up to 68%. So far, the easiest method for stretchability measurement involves *in situ* electrical resistance measurement on graphene while stretching the substrate. Stretchability can be identified as the strain when the resistance of deformed graphene normalized by the undeformed graphene (R/R_0) reaches 10 or 20. The biggest discrepancy comes from the different strain quantification methods for graphene. It is well known that generally, graphene has weak interaction with the underlying substrate and hence can easily slide against the substrate when the substrate is deformed [48–51]. As a result, the strain transfer from substrate to graphene can be very limited and vary significantly from case to case [52, 53]. The interface sliding may lead to higher apparent stretchability for unclamped graphene when substrate strain is used to report stretchability [38–40]. By contrast, when graphene is clamped end-to-end [41, 42] or local strain in graphene is measured using digital image correlation (DIC) method [43], the reported stretchability of graphene is limited to 10%. So far, only polymer substrates with hundred-micron thickness have been

used. However, with the emergence of epidermal electronics such as the graphene electronic tattoos (GETs) [54, 55], graphene can be supported by much thinner substrates such as submicron-thick poly(methyl methacrylate) (PMMA) to achieve ultimate conformability and imperceptibility on human skin. The stretchability and failure mechanism of such graphene-on-ultrathin-PMMA are still unclear. Moreover, graphene has to make electrical contacts with other conductors in practice but the stretchability of such contacts has never been investigated.

Herein, we fabricated monolayer CVD graphene on 300 nm-thick PMMA substrate, which has been successfully applied as GETs [54, 55]. Due to the ultrathin nature of the specimen, we placed the Gr/PMMA ribbon on a soft 3M Tegaderm tape for easier handling. We clamped and stretched four straight Gr/PMMA ribbons uniaxially with *in situ* electrical resistance measurement. Using $R/R_0 = 20$ as the criterion to extract stretchability, our Gr/PMMA stretchability was measured to be $14.5\% \pm 1.1\%$, 45% higher than previously reported stretchability of Gr/PET specimens [42]. For microstructure characterization, we used *in situ* Raman spectroscopy and high-power optical microscope. Four different stages of deformation and fracture can be clearly identified combining the electrical resistance measurements and microstructure analysis. To investigate the stretchability of electrical contacts with graphene, we laminated gold/polyethylene terephthalate (Au/PET) or Gr/PMMA over Gr/PMMA and conducted electromechanical measurements and microstructure examination similar to the Gr/PMMA ribbons. We found very distinct behaviors for those two different types of electrical contacts. We also carried out cyclic tests on Gr/PMMA under small and large strain levels and studied the effects of PMMA thickness and Tegaderm adhesive.

This paper is organized as follows. Section 2 provides the main results regarding specimen fabrication, electromechanical tests, semi-*in situ* microstructure analysis, and the stretchability of electrical contacts of Gr/PMMA. Section 3 discusses the cyclic behavior under small (2%) and large (8%) strains, the effect of PMMA thickness, and the effect of Tegaderm adhesive. Concluding remarks are offered in section 4. Section 5 has more detailed information on the experimental methods. This paper is also supported by ten supplementary figures and three supplementary videos.

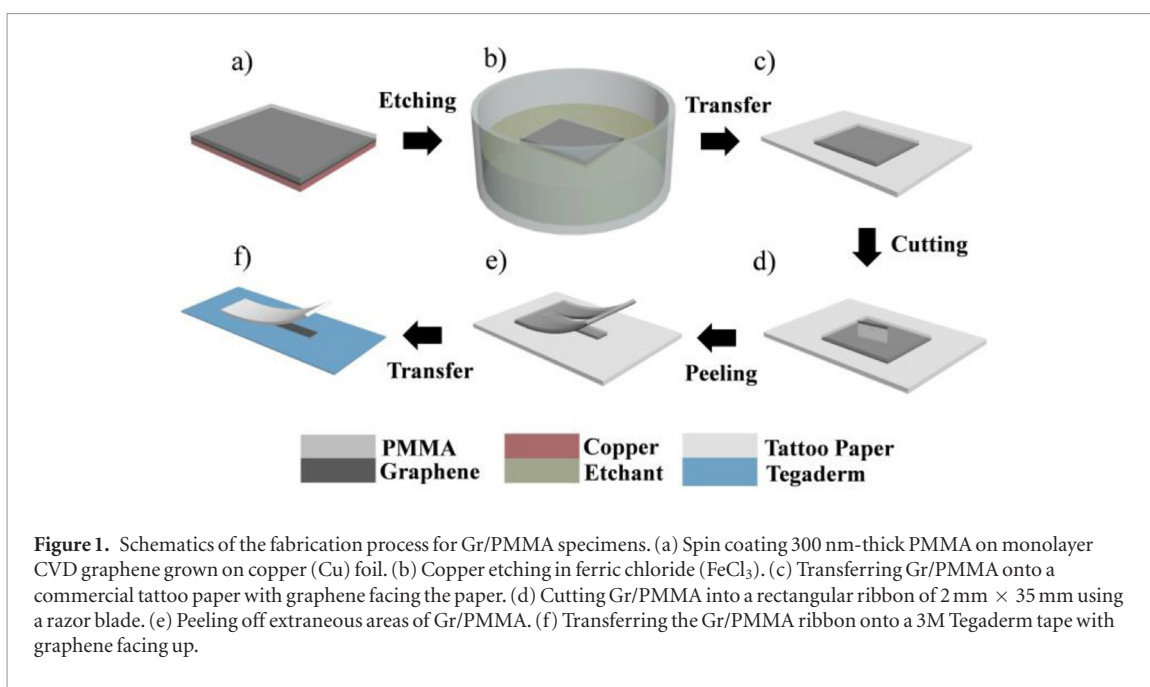
2. Results

2.1. Fabrication of Gr/PMMA specimen

Large area CVD monolayer graphene grown on copper (Cu) foil was obtained from Chongqing Graphene Tech Co. To confirm the continuity of the monolayer graphene, Raman spectra of randomly chosen spots on the as purchased graphene and Raman mapping on a large area ($80 \mu\text{m} \times 80 \mu\text{m}$) were performed and the I_{2D}/I_G ratio was identified (figure S1 (stacks.iop.org/

Table 1. A survey of the stretchability of CVD graphene on different polymer substrates under different strain quantification methods [38–44].

References	Substrate	# of layers of CVD graphene	Strain quantification method	Criteria of stretchability	Stretchability
Kim <i>et al</i> [40]	PDMS	1	Graphene NOT clamped end-to-end	Failure (no $R \sim \varepsilon$ curve)	6%
Verma <i>et al</i> [38]	50 μm PET	1	Graphene NOT clamped end-to-end	$R/R_0 = 10$	~42%
Lee <i>et al</i> [41]	PDMS	3	Graphene clamped end-to-end	Comparable mobilities of electrons and holes (no $R \sim \varepsilon$ curve)	5%
Won <i>et al</i> [43]	188 μm PET	1	Graphene strain measured by DIC	$(R - R_0)/R_0 = 10$	4.5%
Lee <i>et al</i> [42]	188 μm PET	1	Graphene clamped end-to-end	$R/R_0 = 20$	10%
Liu <i>et al</i> [44]	0.1 mm SEBS	1 2 3	Specimen mounting and strain definition unclear	$R/R_0 = 20$	~30% ~58% ~68%
Chun <i>et al</i> [39]	120 μm PDMS	1	Graphene NOT clamped end-to-end	$\Delta R/R_0 \sim 8.5$	20%
Current work	300 nm PMMA on 47 μm Tegaderm	1	Graphene clamped end-to-end	$R/R_0 = 20$	$14.5\% \pm 1.1\%$



TDM/7/014003/mmedia)). The monolayer coverage was measured to be 97.9%, which is comparable with other lab-grown CVD monolayer graphene [21, 56, 57]. According to the graphene manufacturer, the grains size of this CVD graphene is $3\text{--}8\ \mu\text{m}$ (figure S2). The fabrication process of the testing specimen is illustrated in figure 1. First, 300 nm-thick PMMA was spin-coated and cured on as-purchased CVD graphene on Cu foil (figure 1(a)). The specimen was then placed in ferric chloride (FeCl_3) for Cu etching (figure 1(b)) and transferred onto a commercial tattoo paper (Temporary tattoo paper, Silhouette) (figure 1(c)) which allows easy transfer and printing of Gr/PMMA onto arbitrary substrates. A razor blade was used to press-cut the Gr/PMMA sheet into a rectangular ribbon of $2\text{ mm} \times 35\text{ mm}$ (figure 1(d)). Then, the extraneous area was manually peeled off using tweezers (figure 1(e)). The Gr/PMMA ribbon was transferred onto a $47\ \mu\text{m}$ -thick stretchable substrate, the 3M Tegaderm tape (figure 1(f)). The sheet resistance of the transferred specimen was measured to be $1291 \pm 7.9\ \Omega\ \text{sq}^{-1}$, which is comparable to the sheet resistance of many monolayer CVD graphene transferred on foreign substrates in the literature [38, 44, 58]. More details in graphene characterization and specimen preparation can be found in section 5.

2.2. Stretchability and electromechanical behavior of Gr/PMMA ribbons

To investigate the stretchability and electromechanical behaviors of Gr/PMMA ribbons, we used a homemade stretcher with gear motor (TS-32GZ370-5300, Tsiny) to apply uniaxial tension and a data acquisition (DAQ) system (NI Elvis II) to measure electrical resistance *in situ* (figure 2(a)). The Gr/PMMA ribbon supported by a 3M Tegaderm tape was clamped end-to-end to ensure that the applied strain was completely imposed on the ribbon specimen. The metal-based clamps

of the stretcher were covered by double-sided tape (DST) for electrical insulation and mechanical buffer between the rigid clamps and the Gr/PMMA ribbon. The adhesive on the DST prevented the slippage of the specimen during tension. Two flexible Au/PET (100 nm-thick Au on $12.7\ \mu\text{m}$ -thick PET) ribbons were clamped together with Gr/PMMA at each end with Au touching graphene and alligator clips directly clipped on the extended parts of the Au/PET ribbons. The gauge length was 25 mm and the Gr/PMMA and Tegaderm width was 2 mm and 25 mm, respectively. The specimen was stretched uniaxially under a strain rate of $5.2 \times 10^{-4}\ \text{s}^{-1}$. According to a two dimensional (2D) finite element analysis (FEA) of an assumed intact specimen (with Tegaderm) subjected to applied strains up to 20%, the majority of the Gr/PMMA ribbon undergoes uniform uniaxial strain as large as the applied strain (figure S3). It implies that such experimental set up allows almost all applied strains to be imposed on the ribbon specimen if the specimen were not cracking.

The electromechanical results of the uniaxial tensile tests are presented in figure 2(b), which plots the electrical resistance of the graphene ribbon normalized by its initial resistance (R/R_0) as a function of the applied strain till the ribbon fully fractures, i.e. when the resistance blows up. Raw data is plotted as the black curve. Fluctuations in the raw data could result from cracking in graphene. The raw data represented by the black curve was smoothed out to be the red curve using an adjacent-averaging method. Experimentally measured R/R_0 versus ε_{app} curves of three more specimens are offered in figure S4. They show similar characteristics with the curve in figure 2(b) but have slightly different rupture strains. If we define stretchability using the criterion $R/R_0 = 20$, the average stretchability of the four Gr/PMMA ribbons we tested is 14.5% with a standard deviation of 1.1%. It is 45% higher than pre-

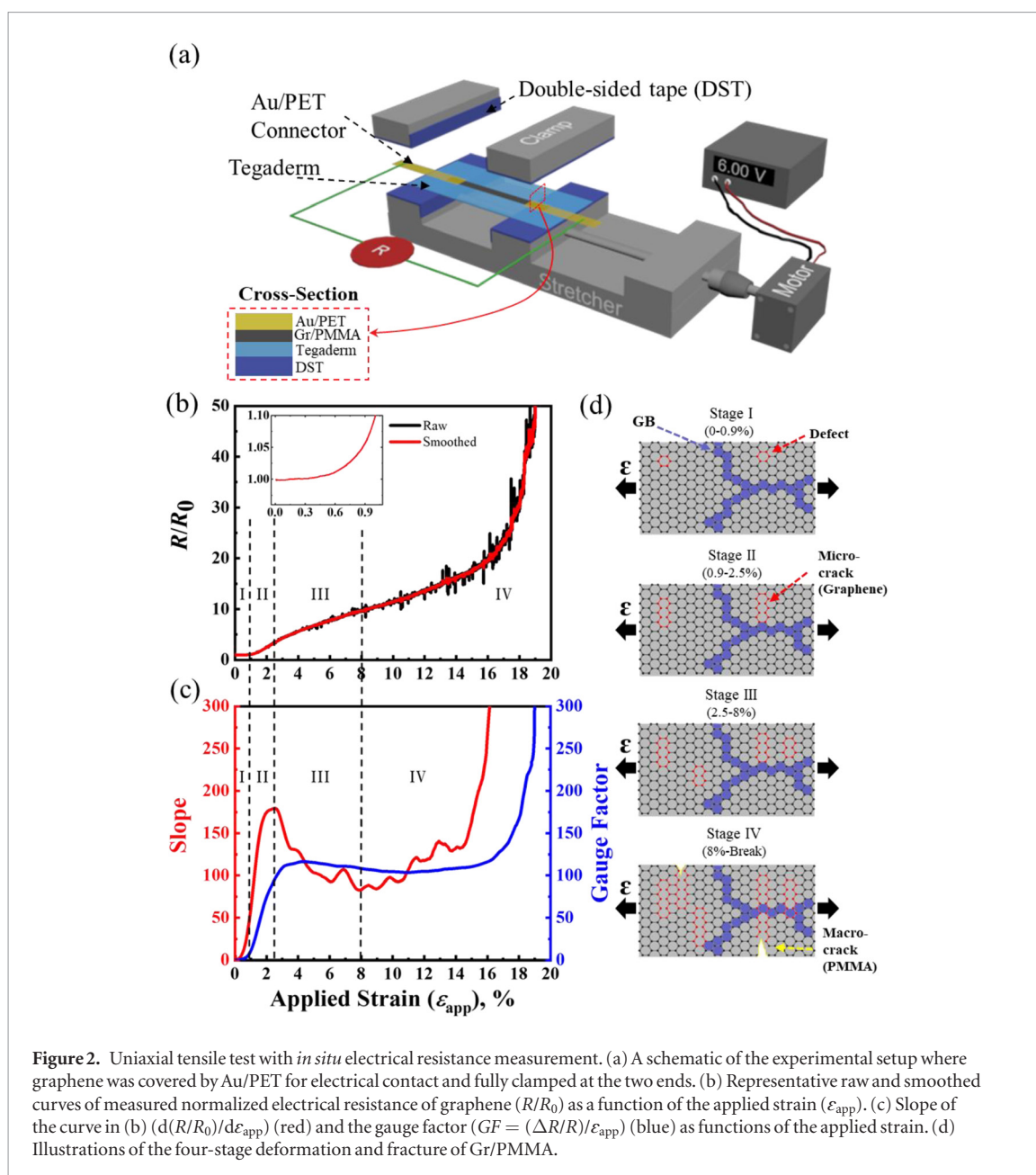


Figure 2. Uniaxial tensile test with *in situ* electrical resistance measurement. (a) A schematic of the experimental setup where graphene was covered by Au/PET for electrical contact and fully clamped at the two ends. (b) Representative raw and smoothed curves of measured normalized electrical resistance of graphene (R/R_0) as a function of the applied strain (ε_{app}). (c) Slope of the curve in (b) ($d(R/R_0)/d\varepsilon_{app}$) (red) and the gauge factor ($GF = (\Delta R/R)/\varepsilon_{app}$) (blue) as functions of the applied strain. (d) Illustrations of the four-stage deformation and fracture of Gr/PMMA.

viously reported Gr/PET specimens under the same criterion [42, 43] and the explanation will be offered after examining the microstructures of the deformed specimens. In figure 2(c), the slope of the smoothed R/R_0 versus ε_{app} curve defined as $d(R/R_0)/d\varepsilon_{app}$ is plotted as the red curve and the widely used gauge factor $GF = (\Delta R/R_0)/\varepsilon_{app}$ is plotted as the blue curve although GF does not mean much for a nonlinear R/R_0 versus ε_{app} curve. Despite the continuous growth of graphene resistance, the slope of the resistance curve is nonmonotonic. Focusing on the red curve in figure 2(c), the slope starts from 0 but grows rapidly till an applied strain of 2.5% where the slope starts to decrease. The slope exhibits a U-shape till an applied strain of 15% where rapid growth kicks in again. Combining the slope analysis and the microstructure analysis in the next section, we have characterized the Gr/PMMA deformation and fracture process into four distinct stages as illustrated in figure 2(d). Stage

I (0%–0.9%) is the pre-cracking elastic deformation stage and grain boundaries (blue) and defects (red) in graphene are illustrated. Stage II (0.9%–2.5%) is the stage when limited number of micro-cracks appear and grow to a limited length ($\sim 3 \mu\text{m}$) in graphene and then halted, which is therefore named the ‘stage of limited micro-cracking in graphene’. Stage III (2.5%–8%) is the stage when many new micro-cracks initiate and grow in graphene, which is therefore called the ‘stage of extensive cracking in graphene’. Stage IV (>8%) is the stage of macro-cracking of PMMA and hence graphene till a complete electrical failure. In Stage IV, the raw resistance curve (black curve in figure 2(b)) exhibits increasing fluctuation possible due to the macro-cracking of PMMA and hence graphene. The argument for Stages II and III comes from a previous stretchability study of monolayer CVD graphene on PET [42]. Through a careful study of how crack length and crack number evolve with strain, it concluded that

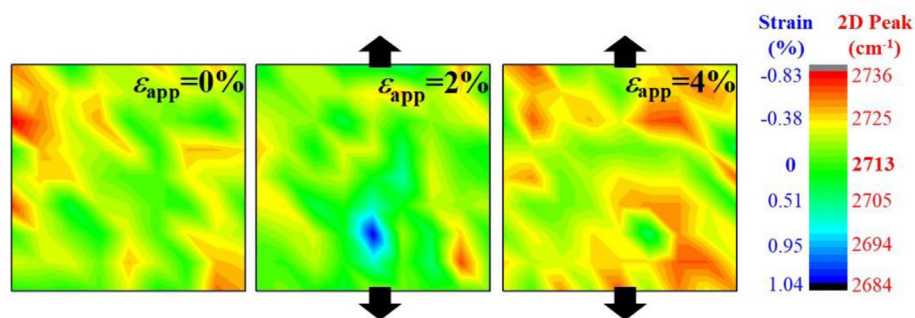


Figure 3. Raman mapping over $20\ \mu\text{m} \times 20\ \mu\text{m}$ graphene at 0%, 2% and 4% of applied strains. Black arrows indicate the direction of stretching. Blueshift and redshift indicate tension and compression, respectively.

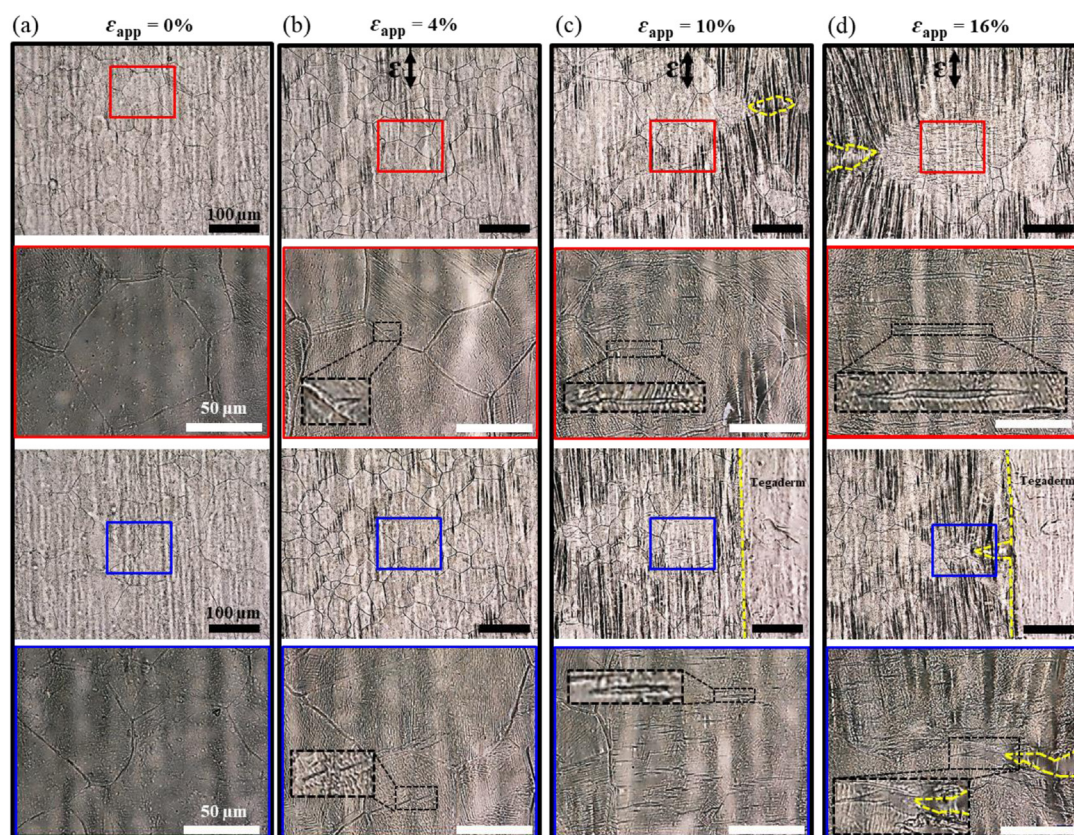


Figure 4. High-power optical micrographs of the Gr/PMMA under $500\times$ (first and third rows) and $2000\times$ (second and fourth rows) magnifications at (a) 0%, (b) 4%, (c) 10% and (d) 16% of applied strains (ϵ_{app}). Tensile strain was applied along the vertical direction of the micrographs. Yellow dashed lines highlight the edges of PMMA. Black boxes offer blown-up views of graphene cracks.

micro-cracks in graphene start to form at $\sim 1\%$ and they grow to a critical size ($\sim 3\ \mu\text{m}$) at $\sim 2.5\%$; beyond 2.5%, existing cracks stop growing but new cracks start to initiate and grow; beyond 8%, many cracks grow beyond $3\ \mu\text{m}$. In the next section, we will present our own semi-*in situ* Raman and optical micrographs to further justify our proposed four-stage deformation and failure of Gr/PMMA, especially at large strains.

2.3. Microstructure analysis of Gr/PMMA

To understand the measured change of resistance during the stretch, we carried out *in situ* microstructure analysis by Raman mapping and high

power optical microscope. The measurements were performed by placing the specimen on a customized low-profile stretcher directly under Raman and optical microscopes. Figure 3 offers the Raman mapping results within one grain of the graphene ($20\ \mu\text{m} \times 20\ \mu\text{m}$) at applied strains 0%, 2% and 4%. The 2D peak position of undeformed graphene was found to be $2713\ \text{cm}^{-1}$ from figure S1, and it was used as the 2D peak position at 0% of the applied strain. The 2D peak shift was converted to uniaxial strain using their linear relationship [59] and both are labeled in the color code of figure 3. According to the Raman mapping, redshifts of 2D peak were present on the

graphene from the beginning, which corresponds to an average compressive strain of 0.24%. This residual compressive strain could be attributed to the transfer or specimen mounting processes. Under 2% of applied strain, the average strain in graphene became 0.083% in compression and some region of graphene was stretched up to 1.04% of strain in tension, implying that overall the graphene layer was stretched but the applied strain was not fully experienced by the graphene. As graphene was clamped end-to-end, the small strain in graphene can be attributed to three possible mechanisms: (1) flattening of ripples, (2) the micro-cracking in graphene, and (3) graphene sliding against PMMA. As the applied strain further increased, however, average strain in graphene dropped to 0.32% in compression possibly due to more significant sliding.

For optical microscopic analysis, we first confirmed that graphene near the edges of the grippers did not crack before the central region and thereafter we always focused our observation around the central region of the specimen. At large strains, we identified two distinct types of cracks, the micro-cracks of graphene and the macro-cracks of PMMA, employing the contrast difference in the optical micrographs under high magnifications (figures 4, S5–S8, and supplementary videos 1–3). Among many micrographs with repetitive behaviors, figure 4 showcases the representative micrographs of the Gr/PMMA ribbon under different strain levels. Two sets of micrographs of unstretched graphene (0%) are exhibited in figure 4(a). The small boxes indicate the regions to be magnified and the corresponding blown-up views are located right below. Although full of ripples inherited from the grain boundaries of the growth Cu foil, no cracks can be observed in graphene at 0%. When the Gr/PMMA ribbon was stretched vertically by 4%, micro-cracks of graphene in the size of tens of microns became visible in the black dashed boxes within the magnified views (figure 4(b)). At higher applied strains (10% and 16%), macro-cracks of 300 nm-thick PMMA in the size of sub-millimeters were observable and the yellow dashed lines highlight the macro-crack and edge of PMMA (figure 4(c)). At a given applied strain, the micro-cracks of the graphene are bigger and denser near the crack tips of PMMA, which is evidenced in supplementary videos 1 and 2. They further grew with increasing applied strain (figures 4(c) and (d)). As electrical current can still flow through the Gr/PMMA ribbon as long as a conductive path can be found, electrical resistance was still measurable even with those micro- and macro-cracks. Finally, the macro-cracks interconnected with each other, forming a complete transverse rupture of the whole ribbon, which completely cut off the current flow and killed the electrical resistance.

Combining the microstructure analysis with the electromechanical measurement results in section 2.1, we are able to classify and justify the deformation and

fracture of the Gr/PMMA ribbon into four distinct stages as illustrated by the schematics in figure 2(d). Stage I is before the applied strain reaches 0.9%, up to which point there is no significant change in resistance. We hypothesize that the compressive residual strain in the unstretched graphene during the wet-etch and transfer process releases in this stage [60] and initial ripples in the specimen get flattened, and therefore the resistance change is insignificant. Although the grain boundaries (GBs) of the graphene are represented by blue hexagons for Stage I schematic in figure 2(d), in reality, the GBs should be misoriented and overlapped [34]. Moreover, structural defects such as the non-homogenous size of the carbon hexagons and irregular geometrical shapes (polygons) are not reflected in this schematic. Getting into Stage II, the resistance elevates rapidly up to 2.5% of applied strain possibly due to the formation of similar-sized micro-cracks in graphene as illustrated by the red-highlighted zones in Stage II schematic of figure 2(d) according to [42]. From 2.5% to 8%, in Stage III, the slope of R/R_0 versus ε_{app} curve decreases as a result of substantial strain relaxation due to sliding [42], despite the initiation and growth of new micro-cracks as illustrated in Stage III schematic of figure 2(d). Beyond 8% is Stage IV, where the slope of R/R_0 versus ε_{app} curve starts to increase due to the macro-cracking of PMMA and hence graphene as illustrated by figure 2(d) Stage IV schematic. This statement is supported by micrographs in figures 4(c) and (d), supplementary figures S5–S8, and supplementary videos 1–3. The resistance increases abruptly beyond 14.5% and the ribbon breaks completely around 19% of the applied strain. Based on a consistent fracture criterion, i.e. $R/R_0 = 20$, the stretchability of our Gr/PMMA ribbon is $14.5\% \pm 1.1\%$, 45% higher than that of PET-supported graphene [42]. The enhancement in stretchability can be attributed to the macro-cracks in PMMA. In fact, strategically designed cuts have been intentionally fabricated in kirigami nanocomposites [61] and auxetic metamaterials [62] to enhance their stretchability. This is because the tensile displacement can be accommodated by the opening of the pre-engineered cuts, which helps release strain in the intact region of the specimen. Based on our repeatability test over four different specimens (figure S4), the strain levels defining the stages vary a bit from specimen to specimen. Such variation can be attributed to the different microscopic and macroscopic defects in graphene caused by the CVD growing process, the metal etching process, the wet transfer process, the push-cut process, the final pasting process and/or the specimen mounting process.

As micro-cracks in graphene initiate at 0.9%, the three R/R_0 versus ε_{app} loading-unloading curves in figure S9 are all irreversible. The extensive sliding between Gr and PMMA at large strains further enlarges the hysteresis in the loading-unloading curves. The cyclic behaviors of Gr/PMMA ribbons will be discussed in section 3.

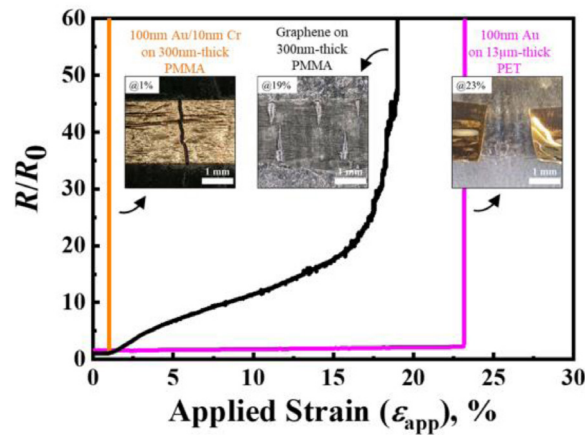


Figure 5. Normalized electrical resistance of Gr/PMMA (black), Au/Cr/PMMA (orange), and Au/PET (magenta) ribbons plotted together against the applied strain. The three insets display the center region of the Au/Cr/PMMA, Gr/PMMA and Au/PET specimens at failure.

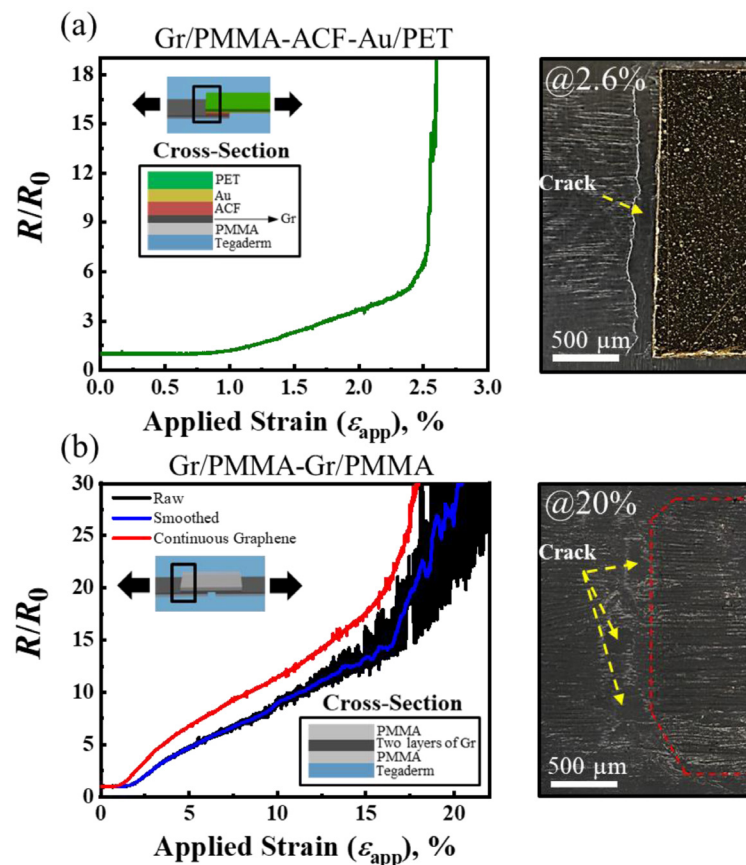


Figure 6. The stretchability of electrical contacts with Gr/PMMA. (a) Au/PET and (b) Gr/PMMA overlayer laminated on Gr/PMMA with Au or graphene facing graphene to make electrical contacts. Au/PET was attached to Gr/PMMA through ACF adhesive but nothing was applied between two Gr/PMMA. The left panels plot the normalized end-to-end electrical resistance versus applied strain. Right panels are micrographs at the edge of the contact taken at the fracture point. Red dashed line in the micrograph of (b) highlights the edge of the top Gr/PMMA.

2.4. Stretchability of electrical contacts with Gr/PMMA

In practice, graphene-based devices such as the graphene e-tattoos (GETs) [54, 55] have to connect with readout circuits through electrical contacts. Therefore, we tried to find out the stretchability of the electrical contacts with our Gr/PMMA ribbon.

Two Au specimens were prepared through thermal evaporation and stretched to find out their intrinsic stretchability before contacting with graphene. The first Au specimen was 100-nm-thick Au on 10 nm-thick Cr on 300 nm-thick PMMA (Au/Cr/PMMA) which is the same PMMA as in the Gr/PMMA specimen. The second Au specimen was 100 nm-thick

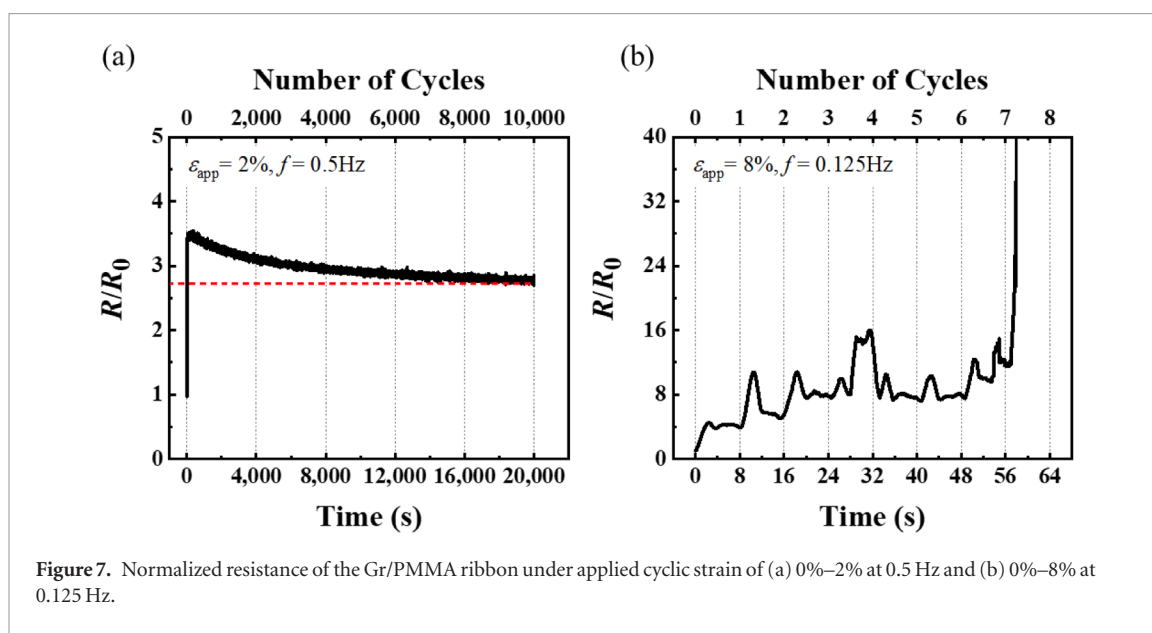


Figure 7. Normalized resistance of the Gr/PMMA ribbon under applied cyclic strain of (a) 0%–2% at 0.5 Hz and (b) 0%–8% at 0.125 Hz.

Au on 13 μm -thick PET (Au/PET). Both of them were prepared to have the same in-plane dimensions as the Gr/PMMA specimens and measured the same way as the Gr/PMMA specimens. Their R/R_0 versus ε_{app} curves are plotted together with the Gr/PMMA one in figure 5. It is evident that the Au/Cr/PMMA specimen fully ruptured at 1% whereas the Au/PET specimen failed at $\sim 23\%$. This is consistent with the previous finding that the thicker and stiffer substrate better spreads the strain in the metal thin film hence affords much higher stretchability [63]. As a result, we chose the Au/PET ribbon to make electrical contact with Gr/PMMA because it is much more robust than the Au/Cr/PMMA and the Gr/PMMA specimen. Of course one can also use other stretchable electrical connectors based on PEDOT:PSS or polymer doped with AgNWs, CNTs, metal nanoparticles, etc [64, 65].

The stretchability of electrical contacts with Gr/PMMA is presented in figure 6. The 3D inset in figure 6(a) left panel illustrates the electrical contact between Gr/PMMA and Au/PET. An anisotropic conductive film (ACF, 3M 9703) was applied between graphene and Au for secure bonding. Uniaxial tension with *in situ* resistance measurement was carried out for this hybrid specimen and the R/R_0 versus ε_{app} curve is plotted in figure 6(a) left panel. The micrograph of the interface at the fracture point (2.6%) is provided in the right panel of figure 6(a). It is evident that the Gr/PMMA ribbon ruptured along the edge of the Au/PET ribbon due to the significant mismatch in mechanical stiffness— 1.24 N mm^{-1} for Gr/PMMA and 46.9 N mm^{-1} for Au/PET. To minimize the stiffness mismatch, we chose to apply a Gr/PMMA to bridge two disconnected Gr/PMMA ribbons as illustrated by the inset in figure 6(b) left panel. The Gr/PMMA ribbon was thin enough to make electrical contact with another Gr/PMMA ribbon via just van der Waals forces so no ACF was applied in this case. We will refer this specimen as the bridged Gr/PMMA specimen in

the follows. Figure 6(b) plots the raw and smoothed R/R_0 versus ε_{app} curves for this specimen together with that of a continuous Gr/PMMA specimen for comparison. Despite the large fluctuation in resistance, the bridged Gr/PMMA specimen exhibits slightly higher stretchability than the continuous Gr/PMMA specimen. Both the fluctuation in resistance and the larger stretchability can be attributed to the sliding between lower and upper graphene. Graphene-graphene sliding is easy to occur and has been widely observed and investigated [30, 53, 66, 67]. Both micro- and macro-cracks were visible in the lower Gr/PMMA ribbons and more cracks were concentrated near the edge of the interface as evident in the micrographs offered in the right panel of figure 6(b). Once the resistance started to change under applied strains, it was not reversible due to the crack formations (figure S10). However, compared to the loading and unloading curves of the continuous Gr/PMMA specimen (figure S9), the loading curves of the bridged Gr/PMMA specimen exhibits larger flat regions, which should result from the sliding between the graphene layers [43, 68]. The improved stretchability for Gr/PMMA to Gr/PMMA contact over Gr/PMMA to Au/PET contact demonstrates that minimizing mechanical stiffness mismatch is the key to enhancing the stretchability of such contacts.

3. Discussion

This section will provide some additional information regarding the stretchability of Gr/PMMA: the cyclic behavior, the effect of PMMA thickness, and the effect of Tegaderm adhesive.

3.1. Cyclic behavior of Gr/PMMA

Although the fatigue behavior of graphene composites has been well studied [69–71], the fatigue behavior of graphene on polymer has been rarely discussed [43]. We, therefore, carried out cyclic electromechanical

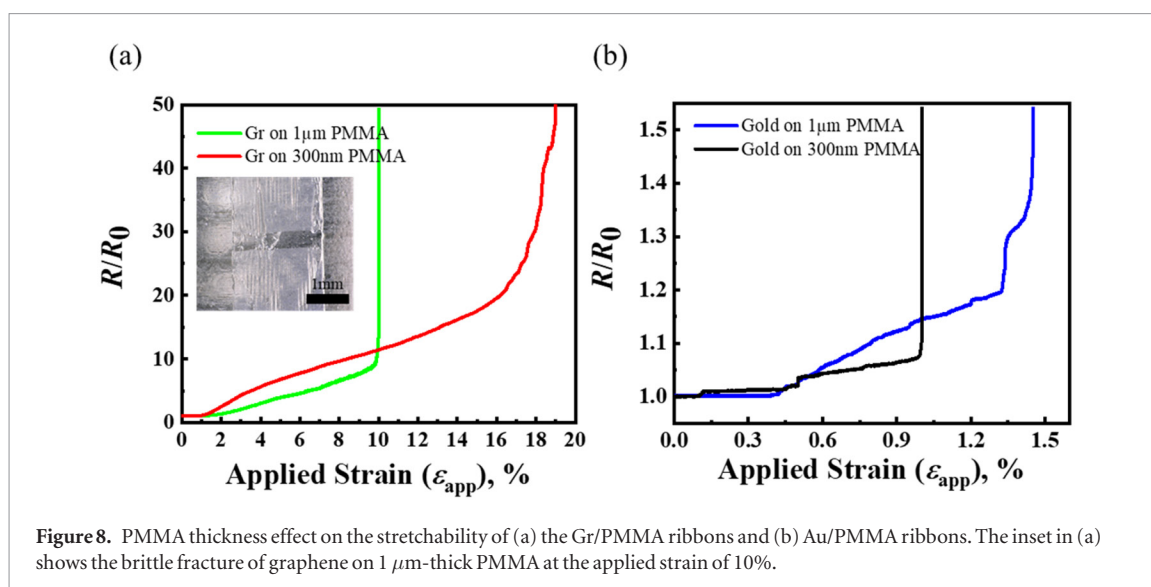


Figure 8. PMMA thickness effect on the stretchability of (a) the Gr/PMMA ribbons and (b) Au/PMMA ribbons. The inset in (a) shows the brittle fracture of graphene on 1 μm -thick PMMA at the applied strain of 10%.

tests on Gr/PMMA ribbons from 0% up to two different strain levels—2% and 8%. The two strain levels represent two different stages in the deformation and failure process—2% is in State II when a limited number of micro-cracks appear in graphene but they tend not to grow beyond 3 μm [42]; 8% is the beginning of Stage IV when macro-cracks in PMMA emerge. The same strain rate of $1 \times 10^{-2} \text{ s}^{-1}$ was applied in both tests. Figure 7 plots the normalized resistance as a function of cyclic time (bottom axis) and number of cycles (top axis). For 2% of applied strain, the resistance of graphene exhibited a sharp rise upon first stretch followed by a gradual decay with growing number of cycles up to 10000 cycles. The reason for such decay in resistance remains elusive for us at this moment. We speculate that it may have something to do with graphene sliding and buckling during the repetitive loading and unloading process. In contrast, the resistance of graphene continued to grow in the cyclic test up to 8% of applied strain and reached complete failure only after the 8th cycle (figure 7(b)). Multiple macro-cracks in PMMA were observable at the failure point. This is consistent with the known fatigue behavior of PMMA [72].

3.2. Effect of PMMA thickness

As a thermoplastic polymer, both ductile and brittle fracture modes exist in PMMA [73]. When the thickness of PMMA is increased, brittle fracture mode is favored [73]. To illustrate the effect of PMMA thickness, we also measured the stretchability of monolayer graphene and 100 nm-thick Au supported by a thicker PMMA (1 μm -thick), and the results are presented in figure 8. In figure 8(a), it is obvious that compared with the stretchability of graphene on 300 nm-thick PMMA (14.5%), the stretchability of graphene on 1 μm -thick PMMA is only 10% and the ribbon was failed by only one straight and brittle crack (inset of figure 8(a)). However, the effect of PMMA thickness on 100-nm-thick Au ribbon is quite the

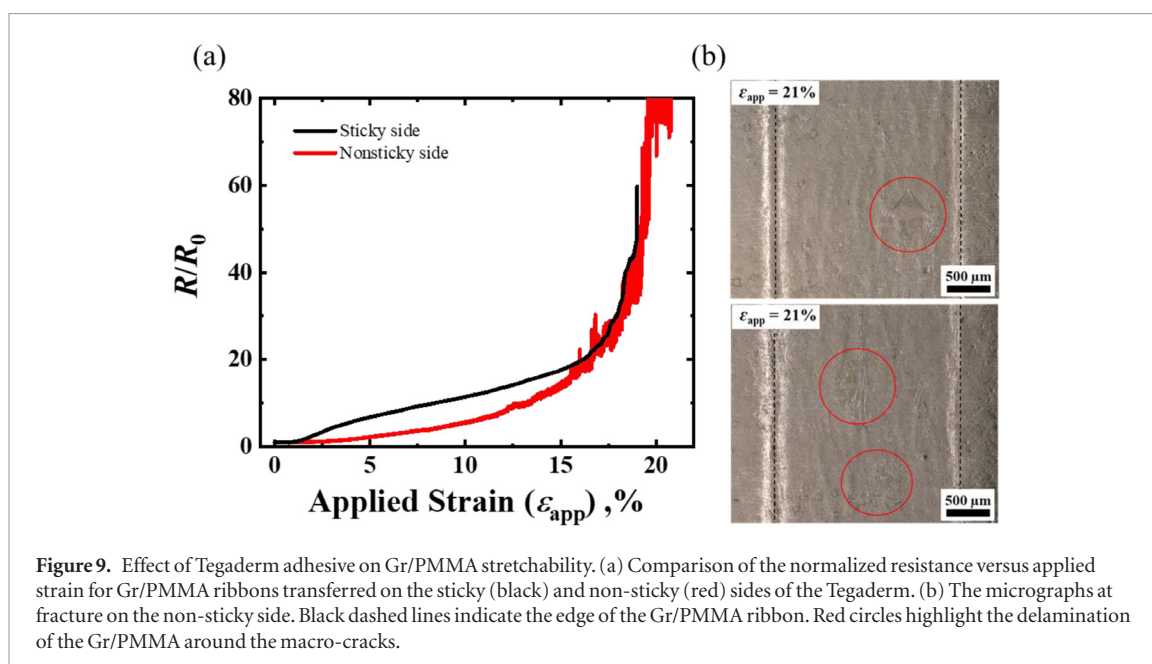
opposite as shown by figure 8(b)—the specimen with 300-nm-thick PMMA ruptured at 1% whereas that with 1 μm -thick PMMA ruptured at 1.4%. This is because both strains are way below the brittle fracture strain of the PMMA. Therefore, according to fracture mechanics of thin films, the thicker PMMA provided more substrate constraint on Au nanomembrane and hence helped enhance its stretchability.

3.3. Effect of the adhesion between Gr/PMMA and substrate

Because our Gr/PMMA ribbon was placed on the native adhesive of the Tegaderm tape, there could be a concern of the adhesive effect. As a result, we carried out a contrast experiment in which case the Gr/PMMA ribbon was transferred to the non-sticky side of Tegaderm. Figure 9(a) plots the R/R_0 versus ϵ_{app} curves of both cases in one chart, which indicates that the stretchability is independent of the adhesive. This finding can be understood as follows. Although the adhesive force is low on the non-sticky side of Tegaderm, the Gr/PMMA ribbon was still able to well conform to the Tegaderm via van der Waals forces due to its thinness (300 nm). Therefore, there was negligible sliding under deformation till macro-cracks appeared in PMMA, where delamination between the ribbon and the Tegaderm substrate was clearly observable at the macro-cracks (figure 9(b)). Because such cracks were sparse, the sliding after such cracking could make very limited contribution to the stretchability.

4. Conclusion

To conclude, we fabricated 300 nm-thick Gr/PMMA ribbons suitable for the applications of stretchable and wearable electronics and measured its stretchability to be $14.5\% \pm 1.1\%$ according to the criterion of $R/R_0 = 20$. The ribbon did not fully rupture until $\sim 19\%$ of the applied strain. Four distinct deformation/



fracture stages were successfully identified when combining the electromechanical measurement with the *in situ* microstructure analysis. Micro-cracks in graphene started to emerge at very low applied strains ($\sim 0.9\%$) and form similar-sized cracks until $\sim 2.5\%$ of the applied strain. After 2.5% of the applied strain, more micro-cracks initiated and propagated. Macro-cracks in PMMA developed after an applied strain of $\sim 8\%$. Both sliding between graphene-PMMA and the macro-cracks in PMMA helped alleviate the tensile stress in graphene, resulting in smaller resistance rise and higher stretchability. But the resistance curves are irreversible due to such cracks. We also investigated the stretchability of different electrical contacts with the Gr/PMMA specimen and concluded that minimizing mechanical stiffness mismatch between the two contacting parts can effectively enhance the stretchability of these contacts. We discovered that Gr/PMMA can be highly cycleable up to 2% but not 8% . Although PMMA thickness has a significant effect on Gr/PMMA stretchability, the Tegaderm adhesive does not. This study provides a comprehensive understanding of the stretchability and fracture behaviors of graphene supported by ultrathin polymer substrates and their electrical contacts. Therefore, it offers useful insights for designing future graphene-based soft electronic devices.

5. Methods

5.1. Characterization of graphene

To verify the quality of the commercially available CVD monolayer graphene on Cu foil from Chongqing Graphene Tech Co. (a.k.a. Moxi Group), the CVD graphene was wet transferred onto a Si wafer and characterized by Renishaw inVia Raman microscope with 442 nm laser (figure S1). To confirm that it is indeed monolayer, the ratio of 2D peak intensity over

G peak intensity (I_{2D}/I_G) was measured and the band shape of 2D peak was verified. The value of I_{2D}/I_G was found out to be higher than 1 and 2D band showed a single peak without splitting [48, 57, 74–76], which are characteristics of monolayer graphene. We obtained a single 2D peak position at three different spots on the graphene as depicted in figure S1(a). Furthermore, we confirmed that the large area of graphene is continuously monolayer via Raman mapping except in a few defected spots (figure S1(b)).

5.2. Fabrication of Gr/PMMA specimen

A CVD monolayer graphene on Cu foil was spin-coated with PMMA (2000 rpm, 45 s; PMMA A4, Microchem). Then, the PMMA/Gr/Cu sheet was immersed in a Cu etchant (CE-100, Trancene) for 1 hour. Afterwards, the graphene layer supported by PMMA (Gr/PMMA) was transferred to DI water and rinsed thoroughly for three times. Temporary tattoo paper (Silhouette temporary tattoo paper, Silhouette) was used to pick up the Gr/PMMA bilayer in DI water and the Gr/PMMA/tattoo paper was dried on a hot plate at $50\text{ }^\circ\text{C}$ for 30 min. The Gr/PMMA on a tattoo paper was manually push-cut into a ribbon shape ($2\text{ mm} \times 35\text{ mm}$) using a razor blade. Then, it was soaked with DI water and excess Gr/PMMA was peeled off from the tattoo paper. After the Gr/PMMA ribbon on a tattoo paper was dried with a nitrogen gun, it was transferred onto the adhesive side of a $47\text{ }\mu\text{m}$ -thick 3M Tegaderm tape.

5.3. Characterization of electromechanical behavior of Gr/PMMA ribbon

The electromechanical behavior of the Gr/PMMA ribbon (25 mm gauge length and 2 mm width) was analyzed using a customized low-profile stretcher integrated with 1 RPM gear motor (TS-32GZ370-5300, Tsiny) (figure 2(a)). The Gr/PMMA ribbon was clamped at both ends with an Au/PET (100 nm -thick

Au on 13 μm -thick PET) ribbon. The clamps of the stretcher were encapsulated by double-sided tapes. The Au/PET connectors were connected to NI ELVIS II (National Instruments Educational Laboratory Virtual Instrumentation Suite) via alligator clips, and the change of resistance was recorded *in situ* via NI LabVIEW with a sampling frequency of 50Hz while the Gr/PMMA ribbon was stretched.

5.4. Microstructure analysis of Gr/PMMA

Raman mapping using Renishaw inVia Raman microscope with 442 nm laser was used to reveal the actual strains experienced by graphene at applied strains up to 4%. To observe micro-cracks of graphene and macro-cracks of PMMA, VHX high-power microscope (VHX-5000, Keyence) was used for capturing the optical micrographs at 500 \times and 2000 \times magnifications at different strain levels.

Acknowledgments

This work is supported by US National Science Foundation (NSF) Grant No. 1738293 and US National Institute of Health (NIH) Grant No. 1R01EB021935-01. The authors would like to thank Dr Krishnaswamy Ravi-Chandar in the Department of Aerospace Engineering and Engineering Mechanics at UT-Austin for allowing us to use the Keyence VHX-5000 digital microscope in his lab. The authors also thank Chongqing Graphene Technology Co. for supplying the CVD graphene and allowing us to use their technical data.

ORCID iDs

Hongwoo Jang  <https://orcid.org/0000-0002-3449-2221>

Zhaohe Dai  <https://orcid.org/0000-0002-5205-089X>

Nanshu Lu  <https://orcid.org/0000-0002-3595-3851>

References

- [1] Koo J H, Kim D C, Shim H J, Kim T-H and Kim D-H 2018 Flexible and stretchable smart display: materials, fabrication, device design, and system integration *Adv. Funct. Mater.* **28** 1801834
- [2] Lu N and Kim D-H 2014 Flexible and stretchable electronics paving the way for soft robotics *Soft Robot.* **1** 53–62
- [3] Rus D and Tolley M T 2015 Design, fabrication and control of soft robots *Nature* **521** 467–75
- [4] Das T, Sharma B K, Katiyar A K and Ahn J-H 2018 Graphene-based flexible and wearable electronics *J. Semicond.* **39** 011007
- [5] Stoppa M and Chiolerio A 2014 Wearable electronics and smart textiles: a critical review *Sensors* **14** 11957–92
- [6] Choi S, Lee H, Ghaffari R, Hyeon T and Kim D-H 2016 Recent advances in flexible and stretchable bio-electronic devices integrated with nanomaterials *Adv. Mater.* **28** 4203–18
- [7] Fan F R, Tang W and Wang Z L 2016 Flexible nanogenerators for energy harvesting and self-powered electronics *Adv. Mater.* **28** 4283–305
- [8] Lu N and Yang S 2015 Mechanics for stretchable sensors *Current Opin. Solid State Mater. Sci.* **19** 149–59
- [9] Yao S and Zhu Y 2015 Nanomaterial-enabled stretchable conductors: strategies, materials and devices *Adv. Mater.* **27** 1480–511
- [10] Cao Q and Rogers J A 2009 Ultrathin films of single-walled carbon nanotubes for electronics and sensors: a review of fundamental and applied aspects *Adv. Mater.* **21** 29–53
- [11] Chae S H and Lee Y H 2014 Carbon nanotubes and graphene towards soft electronics *Nano Convergence* **1** 15
- [12] Dai Z, Liu L, Qi X, Kuang J, Wei Y, Zhu H and Zhang Z 2016 Three-dimensional sponges with super mechanical stability: harnessing true elasticity of individual carbon nanotubes in macroscopic architectures *Sci. Rep.* **6** 18930
- [13] Lee P, Lee J, Lee H, Yeo J, Hong S, Nam K H, Lee D, Lee S S and Ko S H 2012 Highly stretchable and highly conductive metal electrode by very long metal nanowire percolation network *Adv. Mater.* **24** 3326–32
- [14] Langley D, Giusti G, Mayousse C, Celle C, Bellet D and Simonato J-P 2013 Flexible transparent conductive materials based on silver nanowire networks: a review *Nanotechnology* **24** 452001
- [15] Akinwande D, Petrone N and Hone J 2014 Two-dimensional flexible nanoelectronics *Nat. Commun.* **5** 5678
- [16] Zhuang X, Mai Y, Wu D, Zhang F and Feng X 2015 Two-dimensional soft nanomaterials: a fascinating world of materials *Adv. Mater.* **27** 403–27
- [17] Dai Z, Wang Y, Liu L, Liu X, Tan P, Xu Z, Kuang J, Liu Q, Lou J and Zhang Z 2016 Hierarchical graphene-based films with dynamic self-stiffening for biomimetic artificial muscle *Adv. Funct. Mater.* **26** 7003–10
- [18] Lee C, Wei X, Kysar J W and Hone J 2008 Measurement of the elastic properties and intrinsic strength of monolayer graphene *Science* **321** 385–8
- [19] Obraztsov A N 2009 Making graphene on a large scale *Nat. Nanotechnol.* **4** 212–3
- [20] Bae S et al 2010 Roll-to-roll production of 30-inch graphene films for transparent electrodes *Nat. Nanotechnol.* **5** 574–8
- [21] Li X et al 2009 Large area synthesis of high quality and uniform graphene films on copper foils *Science* **324** 1312–4
- [22] Zhu J, Yang D, Yin Z, Yan Q and Zhang H 2014 Graphene and graphene-based materials for energy storage applications *Small* **10** 3480–98
- [23] Jang H, Park Y J, Chen X, Das T, Kim M-S and Ahn J-H 2016 Graphene-based flexible and stretchable electronics *Adv. Mater.* **28** 4184–202
- [24] Ghosh S, Calizo I, Teweldebrhan D, Pokatilov E P, Nika D L, Balandin A A, Bao W, Miao F and Lau C N 2008 Extremely high thermal conductivity of graphene: Prospects for thermal management applications in nanoelectronic circuits *Appl. Phys. Lett.* **92** 151911
- [25] Renteria J, Nika D and Balandin A 2014 Graphene thermal properties: applications in thermal management and energy storage *Appl. Sci.* **4** 525–47
- [26] Shekhawat A and Ritchie R O 2016 Toughness and strength of nanocrystalline graphene *Nat. Commun.* **7** 10546
- [27] Young R J, Liu M, Kinloch I A, Li S, Zhao X, Vallés C and Papageorgiou D G 2018 The mechanics of reinforcement of polymers by graphene nanoplatelets *Compos. Sci. Technol.* **154** 110–6
- [28] Mueller N S et al 2017 Evaluating arbitrary strain configurations and doping in graphene with Raman spectroscopy *2D Mater.* **5** 015016
- [29] Dai Z, Liu L and Zhang Z 2019 Strain engineering of 2D materials: issues and opportunities at the interface *Adv. Mater.* **31** 1805417
- [30] Dai Z, Hou Y, Sanchez D A, Wang G, Brennan C J, Zhang Z, Liu L and Lu N 2018 Interface-governed deformation of nanobubbles and nanotents formed by two-dimensional materials *Phys. Rev. Lett.* **121** 266101
- [31] Iguñiz N, Frisenda R, Bratschitsch R and Castellanos-Gomez A 2019 Revisiting the buckling metrology method to

- determine the Young's modulus of 2D materials *Adv. Mater.* **31** 1807150
- [32] Sgouros A P, Kalosakas G, Galiotis C and Papagelis K 2016 Uniaxial compression of suspended single and multilayer graphenes *2D Mater.* **3** 025033
- [33] Hwangbo Y et al 2015 Fracture characteristics of monolayer CVD-graphene *Sci. Rep.* **4** 4439
- [34] Lee S-M, Kim J-H and Ahn J-H 2015 Graphene as a flexible electronic material: mechanical limitations by defect formation and efforts to overcome *Mater. Today* **18** 336–44
- [35] Wei X, Mao L, Soler-Crespo R A, Paci J T, Huang J, Nguyen S T and Espinosa H D 2015 Plasticity and ductility in graphene oxide through a mechanochemically induced damage tolerance mechanism *Nat. Commun.* **6** 8029
- [36] López-Polín G, Gómez-Herrero J and Gómez-Navarro C 2015 Confining crack propagation in defective graphene *Nano Lett.* **15** 2050–4
- [37] Anagnostopoulos G et al 2016 Mechanical stability of flexible graphene-based displays *ACS Applied Mater. Interfaces* **8** 22605–14
- [38] Verma V P, Das S, Lahiri I and Choi W 2010 Large-area graphene on polymer film for flexible and transparent anode in field emission device *Appl. Phys. Lett.* **96** 203108
- [39] Chun S, Choi Y and Park W 2017 All-graphene strain sensor on soft substrate *Carbon* **116** 753–9
- [40] Kim K S, Zhao Y, Jang H, Lee S Y, Kim J M, Kim K S, Ahn J-H, Kim P, Choi J-Y and Hong B H 2009 Large-scale pattern growth of graphene films for stretchable transparent electrodes *Nature* **457** 706–10
- [41] Lee S-K, Kim B J, Jang H, Yoon S C, Lee C, Hong B H, Rogers J A, Cho J H and Ahn J-H 2011 Stretchable graphene transistors with printed dielectrics and gate electrodes *Nano Lett.* **11** 4642–6
- [42] Lee J H, Jang D W, Hong S G, Park B C, Kim J H, Jung H J and Lee S B 2017 Fracture mechanism and electromechanical behavior of chemical vapor deposited graphene on flexible substrate under tension *Carbon* **118** 475–84
- [43] Won S, Hwangbo Y, Lee S-K, Kim K-S, Kim K-S, Lee S-M, Lee H-J, Ahn J-H, Kim J-H and Lee S-B 2014 Double-layer CVD graphene as stretchable transparent electrodes *Nanoscale* **6** 6057–64
- [44] Liu N et al 2017 Ultratransparent and stretchable graphene electrodes *Sci. Adv.* **3** e1700159
- [45] Chen Z, Xu C, Ma C, Ren W and Cheng H-M 2013 Lightweight and flexible graphene foam composites for high-performance electromagnetic interference shielding *Adv. Mater.* **25** 1296–300
- [46] Yang J, Wei D, Tang L, Song X, Luo W, Chu J, Gao T, Shi H and Du C 2015 Wearable temperature sensor based on graphene nanowalls *RSC Adv.* **5** 25609–15
- [47] Li X, Sun P, Fan L, Zhu M, Wang K, Zhong M, Wei J, Wu D, Cheng Y and Zhu H 2012 Multifunctional graphene woven fabrics *Sci. Rep.* **2** 395
- [48] Gong L, Kinloch I A, Young R J, Riaz I, Jalil R and Novoselov K S 2010 Interfacial stress transfer in a graphene monolayer nanocomposite *Adv. Mater.* **22** 2694–7
- [49] Papageorgiou D G, Kinloch I A and Young R J 2017 Mechanical properties of graphene and graphene-based nanocomposites *Prog. Mater. Sci.* **90** 75–127
- [50] Wang G, Dai Z, Liu L, Hu H, Dai Q and Zhang Z 2016 Tuning the Interfacial mechanical behaviors of monolayer graphene/PMMA nanocomposites *ACS Appl. Mater. Interfaces* **8** 22554–62
- [51] Dai Z, Wang G, Liu L, Hou Y, Wei Y and Zhang Z 2016 Mechanical behavior and properties of hydrogen bonded graphene/polymer nano-interfaces *Compos. Sci. Technol.* **136** 1–9
- [52] Sanchez D A, Dai Z, Wang P, Cantu-Chavez A, Brennan C J, Huang R and Lu N 2018 Mechanics of spontaneously formed nanoblisters trapped by transferred 2D crystals *Proc. Natl Acad. Sci.* **115** 7884–9
- [53] Wang G, Dai Z, Wang Y, Tan P, Liu L, Xu Z, Wei Y, Huang R and Zhang Z 2017 Measuring Interlayer shear stress in bilayer graphene *Phys. Rev. Lett.* **119** 036101
- [54] Kabiri Ameri S, Ho R, Jang H, Tao L, Wang Y, Wang L, Schnyer D M, Akinwande D and Lu N 2017 Graphene electronic tattoo sensors *ACS Nano* **11** 7634–41
- [55] Ameri S K, Kim M, Kuang I A, Perera W K, Alshiekh M, Jeong H, Topcu U, Akinwande D and Lu N 2018 Imperceptible electrooculography graphene sensor system for human–robot interface *npj 2D Mater. Appl.* **2** 19
- [56] Muñoz R and Gómez-Aleixandre C 2013 Review of CVD Synthesis of graphene: review of CVD synthesis of graphene *Chem. Vapor Depos.* **19** 297–322
- [57] Komissarov I V et al 2015 Micro Raman investigation of graphene synthesized by atmospheric pressure CVD on copper foil from decane *Phys. Procedia* **72** 450–4
- [58] Li X, Zhu Y, Cai W, Borysiak M, Han B, Chen D, Piner R D, Colombo L and Ruoff R S 2009 Transfer of large-area graphene films for high-performance transparent conductive electrodes *Nano Lett.* **9** 4359–63
- [59] Ni Z H, Yu T, Lu Y H, Wang Y Y, Feng Y P and Shen Z X 2008 Uniaxial strain on graphene: Raman spectroscopy study and band-gap opening *ACS Nano* **2** 2301–5
- [60] Deng S and Berry V 2016 Wrinkled, rippled and crumpled graphene: an overview of formation mechanism, electronic properties, and applications *Mater. Today* **19** 197–212
- [61] Xu L, Shyu T C and Kotov N A 2017 Origami and kirigami nanocomposites *ACS Nano* **11** 7587–99
- [62] Tang Y and Yin J 2017 Design of cut unit geometry in hierarchical kirigami-based auxetic metamaterials for high stretchability and compressibility *Extreme Mech. Lett.* **12** 77–85
- [63] Li T and Suo Z 2007 Ductility of thin metal films on polymer substrates modulated by interfacial adhesion *Int. J. Solids Struct.* **44** 1696–705
- [64] Yu Z, Niu X, Liu Z and Pei Q 2011 Intrinsically stretchable polymer light-emitting devices using carbon nanotube-polymer composite electrodes *Adv. Mater.* **23** 3989–94
- [65] Wang Y et al 2017 A highly stretchable, transparent, and conductive polymer *Sci. Adv.* **3** e1602076
- [66] Gao W and Tkatchenko A 2015 Sliding mechanisms in multilayered hexagonal boron nitride and graphene: the effects of directionality, thickness, and sliding constraints *Phys. Rev. Lett.* **114** 096101
- [67] Liu Z, Yang J, Grey F, Liu J Z, Liu Y, Wang Y, Yang Y, Cheng Y and Zheng Q 2012 Observation of microscale superlubricity in graphite *Phys. Rev. Lett.* **108** 205503
- [68] Feng X, Kwon S, Park J Y and Salmeron M 2013 Superlubric sliding of graphene nanoflakes on graphene *ACS Nano* **7** 1718–24
- [69] Bortz D R, Heras E G and Martin-Gullon I 2012 Impressive fatigue life and fracture toughness improvements in graphene oxide/epoxy composites *Macromolecules* **45** 238–45
- [70] Rafiee M A, Rafiee J, Srivastava I, Wang Z, Song H, Yu Z-Z and Koratkar N 2010 Fracture and fatigue in graphene nanocomposites *Small* **6** 179–83
- [71] Shen M-Y, Chang T-Y, Hsieh T-H, Li Y-L, Chiang C-L, Yang H and Yip M-C 2013 Mechanical properties and tensile fatigue of graphene nanoplatelets reinforced polymer nanocomposites *J. Nanomater.* **2013** 1–9
- [72] Hoey D and Taylor D 2009 Comparison of the fatigue behaviour of two different forms of PMMA *Fatigue Fract. Eng. Mater. Struct.* **32** 261–9
- [73] Johnson D D 2008 *Illinois MATSE 280: Introduction to Engineering Materials* (<https://nanohub.org/resources/5220>)
- [74] Davaji B, Cho H D, Malakoutian M, Lee J K, Panin G, Kang T W and Lee C H 2017 A patterned single layer graphene resistance temperature sensor *Sci. Rep.* **7** 8811
- [75] Graf D, Molitor F, Ensslin K, Stampfer C, Jungen A, Hierold C and Wirtz L 2006 Spatially resolved Raman spectroscopy of single- and few-layer graphene *Solid State Phys.* **7** 1–6
- [76] Su C Y et al 2011 Direct formation of wafer scale graphene thin layers on insulating substrates by chemical vapor deposition *Nano Lett.* **11** 3612–6

Supporting Information

Stretchability of PMMA-Supported CVD Graphene and of Its Electrical Contacts

Hongwoo Jang¹, Zhaohe Dai², Kyoung-Ho Ha³, Shideh Kabiri Ameri⁴ and Nanshu Lu^{1,2,5}

¹ Texas Materials Institute, University of Texas at Austin, Austin, TX, United States

² Department of Aerospace Engineering and Engineering Mechanics, University of Texas at Austin, Austin, TX, United States

³ Department of Mechanical Engineering, University of Texas at Austin, Austin, TX, United States

⁴ Department of Electrical and Computer Engineering, University of Texas at Austin, Austin, TX, United States (currently at Department of Electrical and Computer Engineering, Queen's University, Kingston, ON, Canada)

⁵ Department of Biomedical Engineering, University of Texas at Austin, Austin, TX, United States

Correspondence: nanshulu@utexas.edu

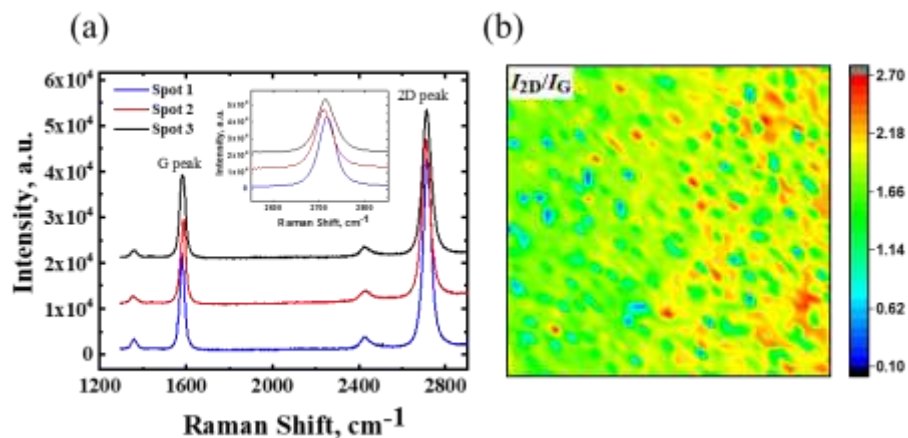


Figure S1. Characterization of commercial CVD-grown graphene under Raman spectroscopy. (a) Three random spots were chosen and the characteristic peaks of the graphene (2D peak and G peak) were measured. The inset figure shows a zoomed-in view of the 2D peaks. (b) Raman mapping was performed within an area of $80\ \mu\text{m} \times 80\ \mu\text{m}$ of the CVD graphene to construct a contour plot of the ratio of 2D peak intensity over G peak intensity (I_{2D}/I_G).

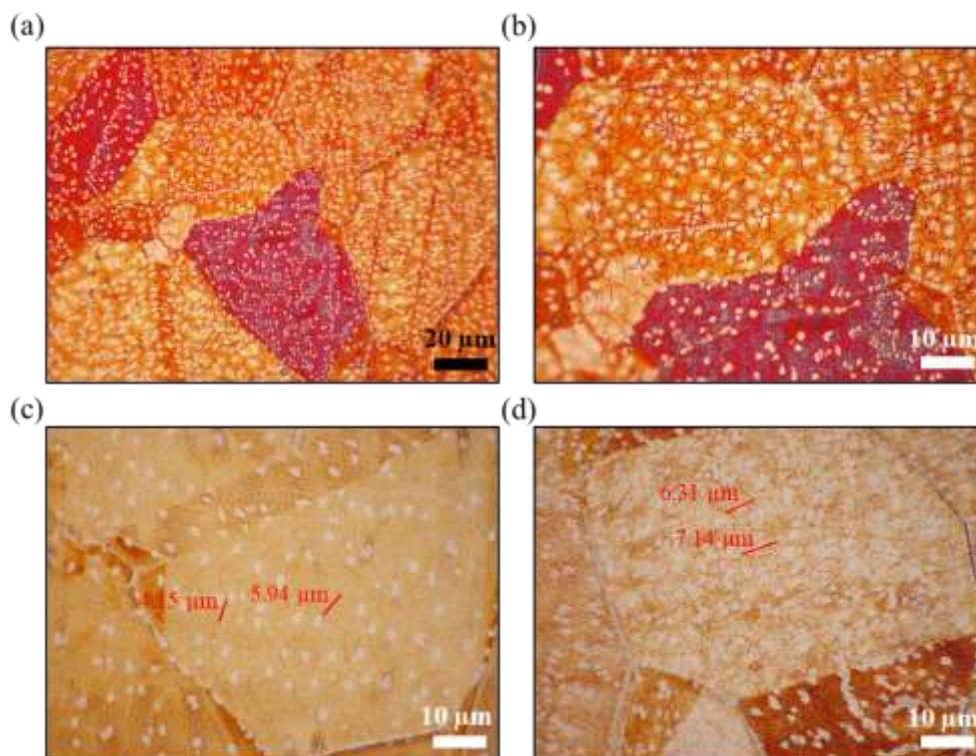


Figure S2. Optical micrographs of the CVD graphene on Cu foil (Gr/Cu) after treating with Ozone. (a) A snapshot of the Gr/Cu, which shows large copper grain boundaries and small graphene grain boundaries (red lines). (b) Zoomed-in view of (a). (c) and (d) shows other regions of the Gr/Cu and some of the grain sizes are labelled.

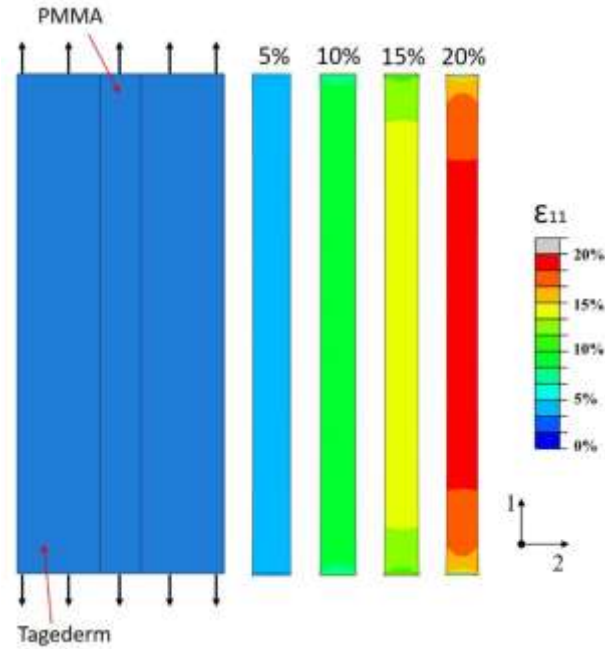


Figure S3. Finite element analysis results of the normal strain in the stretching direction (ϵ_{11}) in the Gr/PMMA ribbon. Note that most of the Gr/PMMA ribbon experiences ϵ_{11} similar to the applied strain.

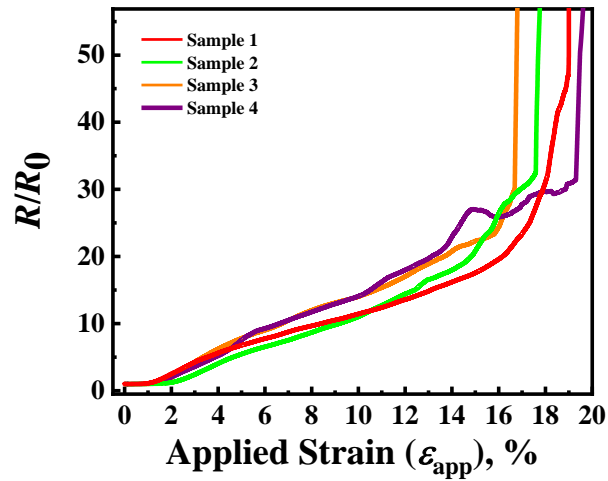


Figure S4. Repeatable electromechanical behavior of four Gr/PMMA ribbons on 3M Tegaderm tapes under tension.

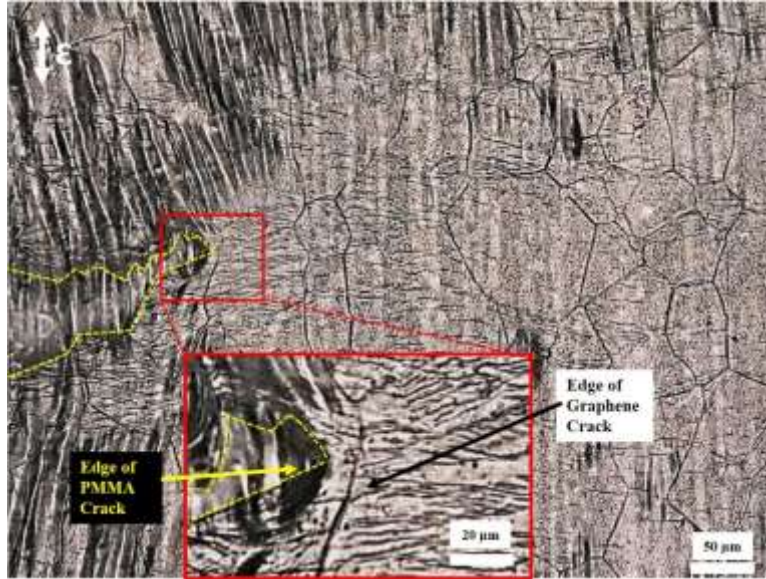


Figure S5. A micrograph of Gr/PMMA on a 3M Tegaderm tape at 16% of applied strain. Macro-cracks of PMMA were generated from the edge and graphene near the PMMA crack tip contained many micro-cracks due to crack tip strain concentration. In contrast, graphene far from the macro-crack of PMMA has fewer and smaller micro-cracks.

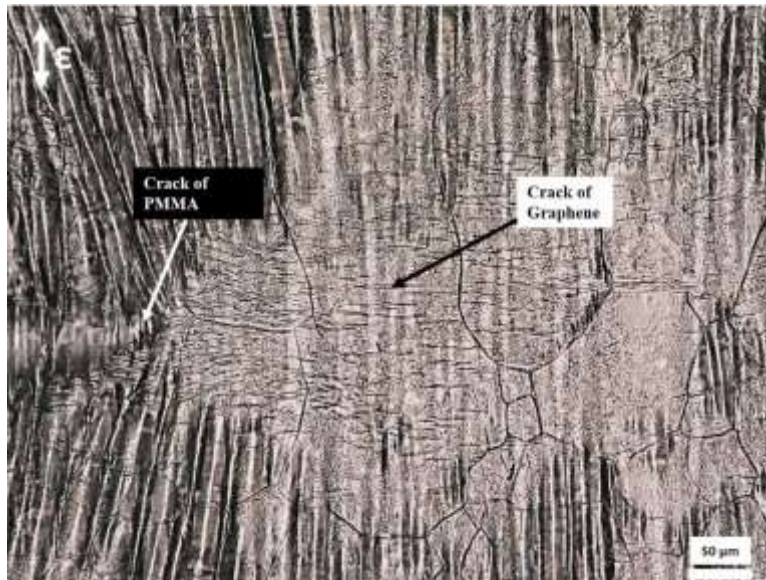


Figure S6. Additional micrograph of Gr/PMMA on a 3M Tegaderm tape at 16% of applied strain.

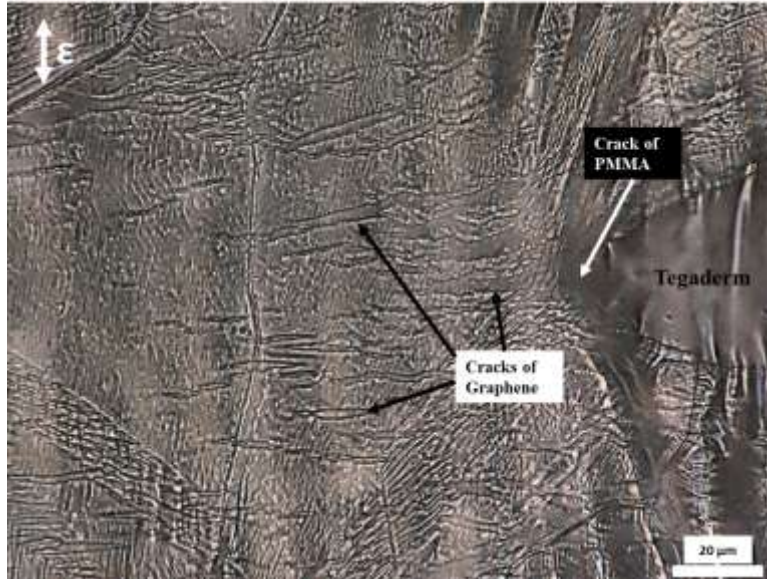


Figure S7. Additional micrograph of Gr/PMMA on a 3M Tegaderm tape at 16% of applied strain.



Figure S8. A global view of a Gr/PMMA ribbon on a 3M Tegaderm tape at fracture (18% of applied strain). Many macro-cracks transverse to the stretching direction are visible.

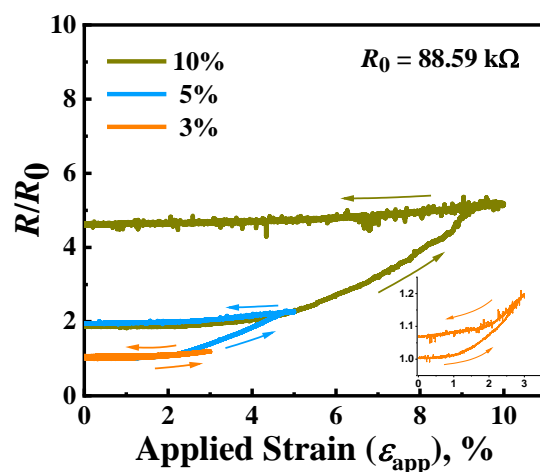


Figure S9. Loading and unloading tests on a Gr/PMMA ribbon supported by a 3M Tegaderm tape at different applied strains. The inset displays the zoomed-in view for the case when loading up to 3% and unloading.

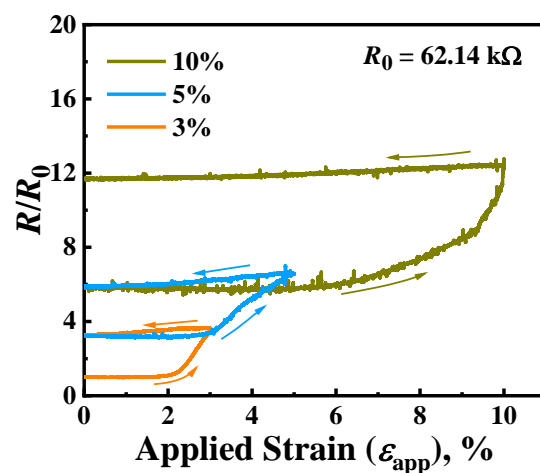


Figure S10. Loading and unloading tests on the bridged Gr/PMMA supported by a 3M Tegaderm tape at different applied strains.

Supplementary Videos. DOI: 10.17632/522dfg82k7.2

(Supplementary Video 1 and Video 2. Crack propagation of the Gr/PMMA ribbon under tension)

(Supplementary Video 3. Initiation of PMMA crack on Gr/PMMA ribbon stretched from 7% to 8.5%)